Loss mechanisms in high efficiency polymer solar cells

R. C. I. MacKenzie[1], V. S. Balderrama[2], S. Schmeisser[3], R. Stoof[4], S. Greedy[1], J. Pallarès[2], L. F. Marsal[2], A. Chanaewa[4], E. von Hauff[4]

[1] Faculty of Engineering, University of Nottingham, Nottingham NG7 2RD, United Kingdom

[2] Departament d'Enginyeria Electrònica Elèctrica i Automàtica, Universitat Rovira i Virgili, Avda. Països Catalans 26, 43007 Tarragona, Spain

[3] Institute of Physics, Albert-Ludwigs University of Freiburg, Hermann-Herder-Str. 3, 79104 Freiburg, Germany

[4] Physics of Energy, Department of Physics and Astronomy, Amsterdam, Netherlands

Device Fabrication

Methods

Materials: ITO-coated glass substrates were purchased from PsiOTec Ltd. PTB7 and PFN materials were purchased from One-Material. $PC_{70}BM$ was purchased from Solenne BV. High-purity (99.99%) silver wire was obtained from Testbourne Ltd.

Device Fabrication: Solar cells were fabricated on pre-cleaned, patterned ITO glass substrates (10 Ω/□). PFN was dissolved in methanol in the presence of a small amount of acetic acid (2 mg/mL) and was spin-coated on top of the pre-cleaned ITO substrate at 3500 rpm for 60 s to achieve 10 nm films. $PTB7:PC_{70}BM$ with a weight ratio of 1:1.5 was dissolved in chlorobenzene (CB) and 1,8-diiodooctane (DIO) (CB:DIO = 97:3 by volume) to achieve a solution with 25 mg/mL and left stirring overnight. Subsequently the solution was stored for 40 h under nitrogen in the dark at room temperature. The blend solution was deposited on the PFN layer by spin coating at 800 rpm for 30 s, obtaining a thickness of 100±5 nm. Film thicknesses were measured by a Dektak 150 surface profilometer. Afterwards, 5 nm of V_2O_5 and 100 nm of Ag were subsequently deposited by thermal evaporation in a vacuum chamber (5 x 10^{-7} mbar), at a rate of 0.05 kÅ/s and 0.1-0.4 kÅ/s, respectively.

Ageing: Solar cells were removed from the glove box after fabrication stored in the cupboard under ambient conditions for over four weeks. After ageing, they were brought back into the glove box for characterization.

Solar cell characterization: Current density-voltage (JV) characteristics (illuminated/dark) using a Keithley 2401 source measurement unit in combination with a solar simulator SS80 (Photo Emission Tech, Inc.). Appropriate filters were used to reproduce the AM 1.5G spectrum. The light intensity (100 mW/cm^2) was calibrated with a calibrated silicon photodiode (Fraunhofer ISE). Impedance spectroscopy and intensity modulated photocurrent spectroscopy were performed with a Metrohm Autolab B. V. and the accompanying software, Nova. Fits of the impedance spectra were performed using Z-View. A red LED (627 nm) was used to provide DC and AC illumination for IMPS measurements. The amplitude of the perturbation intensity was 10% of the DC intensity. Solar cell characterization was performed at room temperature in a nitrogen atmosphere.

Impedance spectroscopy (IS) on fresh and aged devices

Fig S1 shows the equivalent circuit diagram used to fit the impedance spectra, three resistor-capacitance (RC) elements in series[1].
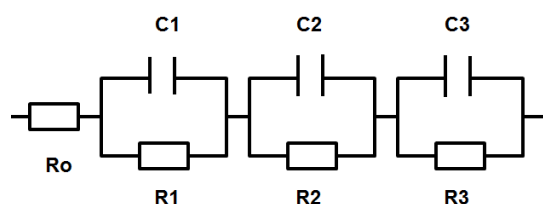

Figure S1 Equivalent circuit diagram used to simulate the impedance data.

The values of the voltage-dependent circuit elements for the solar cell before and after ageing are summarized in table S1. We observe that the resistance changes with applied DC voltage, while the capacitance is voltage-independent. Generally the impedance response is only weakly voltage dependent. These points are consistent with the high FF in these devices.

   We assign the circuit elements to specific sites in the solar cell[2]. R_o represents the voltage-independent contact resistance, and was comparable for the fresh (17.3 Ω) and aged (14.3 Ω) devices. The values for R_1 and C_1 are comparatively large (6 – 8 kΩ), and we attribute this element to the response at the anode interface, while the R_2C_2 element is attributed to the response of the active layer. Finally we attribute the R_3C_3 element to the cathode interface.

   The assignment of the active layer was confirmed by comparing the impedance values of the inverted devices to data taken from solar cells prepared in the standard architecture, i.e. with PEDOT:PSS/ITO anodes and Ca/Al top cathodes. These

devices demonstrated a total device resistance in the order of 500 Ω, indicating that the difference in resistance arises due to the different contacting materials.

The assignment of the R_1C_1 element to the anode interface is consistent with the dark impedance spectra which reveals no signal at the same DC voltages (0 – 0.6 V), indicating a large barrier for carrier injection, consistent with the high turn-on voltages in these devices. While charge extraction under illumination appears to be very efficient in these devices, charge injection is only induced at high positive voltages (> 0.6 V). As PFN is known to be both an efficient electron injection and extraction layer in inverted PTB7:PC_{70}BM solar cells, we attribute the large resistance at positive bias to the V_2O_5 interface.

Table S1. Values of resistors (R) and capacitances (C) used to fit the impedance data for the fresh and aged device at applied voltages of 0 V, 0.4 V, 0.5 V and 0.6 V

Device	Voltage (V)	R_1 (Ω)	C_1 (nF)	R_2 (Ω)	C_2 (nF)	R_3 (Ω)	C_3 (nF)
Fresh	0	8633	6.87	500	38	37	40
	0.4	8309	6.87	441	38	34	40
	0.5	8145	6.87	396	38	32	40
	0.6	7991	6.87	359	38	30	40
Aged	0	6626	7.31	665	31	32	70
	0.4	6856	7.31	677	31	34	70
	0.5	7019	7.31	689	31	34	70
	0.6	7034	7.31	678	31	33	70

Description of the model and simulation parameters

To calculate the electrostatic potential distribution within the device we solve Poisson's equation between the cathode ($x=0$) and the anode ($x=d$),

$$\frac{d}{dx} \varepsilon_0 \varepsilon_r \frac{d}{dx} \varphi = q\left(n_f + n_t - p_f - p_t\right) \qquad (1)$$

where φ is the local electrostatic potential, n_f the density of free electrons, n_t the density of trapped electrons, p_f the density of free holes, p_t the density of trapped holes, and ε_r is the permittivity of the medium. To describe charge carrier transport within the device, the drift and diffusion equations are solved for electrons,

$$J_n = q\mu_e n_f \frac{\partial E_{LUMO}}{\partial x} + qD_n \frac{\partial n_f}{\partial x} \qquad (2)$$

and for holes,

$$J_p = q\mu_h p_f \frac{\partial E_{HOMO}}{\partial x} - qD_p \frac{\partial p_f}{\partial x} \qquad (3)$$

where, J_n is the electron flux, J_p is the hole flux, E_{LUMO} is the electron mobility edge, E_{HOMO} is the hole mobility edge and all other symbols have their usual meanings. To force conservation of particles the electron and hole continuity equations are also solved. It is well known that organic semiconductors are electronically disordered material therefore we include two exponential tails of trap states within the band gap. The distribution of electron trap states in is described using,

$$\rho^e(E) = N^e \exp(E / E_u^e) \qquad (4)$$

and the distribution of hole trap states as,

$$\rho^h(E) = N^h \exp(E / E_h^u) \qquad (5)$$

where, N^e is the magnitude of the trap distribution at the LUMO edge, N^h is the magnitude of the trap distribution at the HOMO edge, and E_u^e is the characteristic energy of the electron trap distribution and E_u^h is the characteristic energy of the hole trap distribution. Each tail of trap states is split up into 20 individual trap levels, each with its own quasi-Fermi level. Capture and escape of charge carriers from each trap level is described using the Shockley-Read-Hall formalism, which accounts for charge carrier recombination via a free carrier to trapped carrier process. A transfer matrix model is used to calculate the optical profile of the light within the device.

It should be noted that the values of mobility μ_0 are values of free carrier mobility and are not averaged over trapped charge carriers. These values compare well with the values of $\mu_{infinity}$ reported in [3].

Parameter	Value	Unit
Electron trap density	1.6×10^{25}	$m^{-3} eV^{-1}$
Hole trap density	1.6×10^{25}	$m^{-3} eV^{-1}$
Electron tail slope	1.1×10^{-01}	eV
Hole tail slope	1.1×10^{-01}	eV
Electron mobility	4.1×10^{-06}	$m^2 V^{-1} s^{-1}$
Hole mobility	4.1×10^{-06}	$m^2 V^{-1} s^{-1}$
Relative permittivity	3	au
Free electron to Trapped electron	1.4×10^{-24}	m^{-2}
Trapped electron to Free hole	9.6×10^{-21}	m^{-2}
Trapped hole to Free electron	4.5×10^{-27}	m^{-2}
Free hole to Trapped hole	1.4×10^{-24}	m^{-2}
Effective density of free electron states	5.0×10^{26}	m^{-2}
Effective density of free hole states	5.0×10^{26}	m^{-2}

Table S2: Simulation parameters obtained from fitting the model to the experimental data.

The model was fit to the illuminated JV curve and two cycles of the IMPS data (2818 Hz and 39.8 Hz). The data were taken under the same illumination conditions, 1 sun at 632 nm.
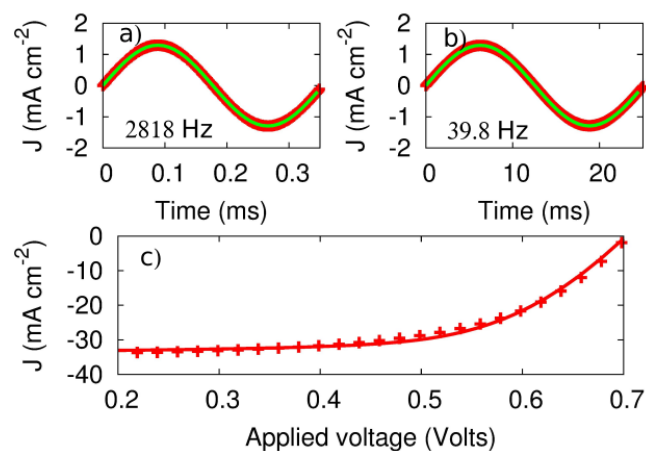

Figure S2 A fit of the model to the illuminated JV curve (100 mW cm^{-2}) and to two cycles of the IMPS data of a fresh device (inset)

Discussion of the peak observed at 3kHz

Figure S3 shows the normalized carrier generation rate (red line), plotted against the normalized density of carriers in trap states. The free carrier population and current from the device closely follow the carrier generation rate (not shown). In this device the recombination cross section is larger than the thermalization cross section, this means that photogenerated electrons (holes) will more readily recombine with trapped holes (electrons) than relax into electron (hole) trap states. This means that, the charge carrier generation rate and the density of trapped carriers are exactly 180 degrees out of phase. This can be seen in figure S3, by comparing the carrier generation rate (red line) and the density of trapped carriers at 15 Hz (green line). As the modulation frequency is increased, recombination effects can no longer keep up with the quickly changing optical field, the population of the trapped carriers, therefore starts to lag the generation rate by more than 180 degrees. This means that the minimum in the population of trapped charges and thus recombination rate shifts to earlier times, making the device more efficient before the peak in the photo current has been reached. This in turns makes the current precede the generation rate.
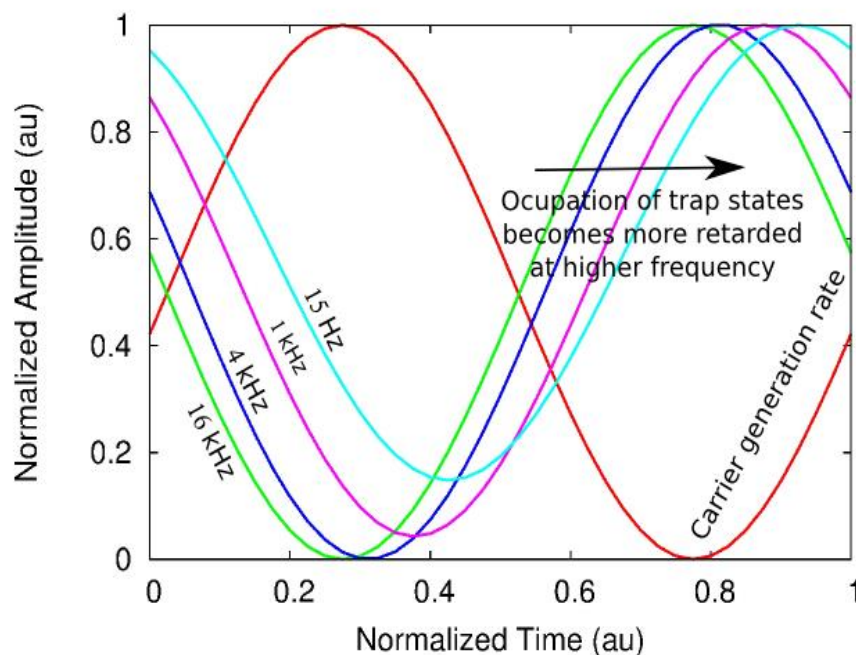

Figure S3 The carrier generation rate (red line), plotted against normalized carrier density in the trap states (green, blue, purple and turquoise)

The roll of band bending in producing a positive IMPS signal.

Figure S4a, plots the imaginary IMPS response of the device as a function of permittivity of the active region. It can be seen that as the permittivity is artificially increased to turn off band bending, the imaginary component of the IMPS spectra between 1 Hz and 10 kHz, reduces becoming zero with a permittivity of 1×10^6. This demonstrates that the positive IMPS response at low frequencies is due to band bending rather than trapping and recombination effects (a detailed examination of the band structure as a function of time supports this). Figure S4b, plots the band bending within the device as a function of frequency. The degree of band bending in the device is described with the equation

$$bandbending(t) = \frac{100}{d} \cdot \int \frac{|\ \phi(x,t)_0 - \phi(x,t)|}{|\phi(x,t)|} dx$$

Where d is the thickness of the active layer, ϕ represents the local potential within the device as a function (x) of position and time (t).

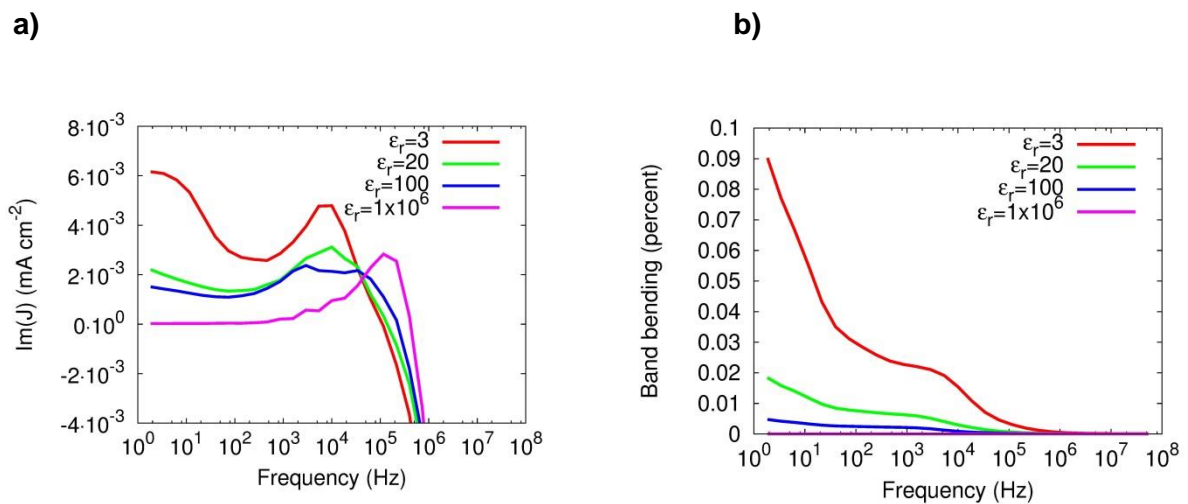a)   b)

Figure S4: a) The imaginary IMPS response as a function of permitivity. b) Band bending characterized by percentage change in the potential profile. It can be seen that as the band bending decreases so does the positive imaginary component of the IMPS signal.

As stated in the main text, we were unable to make the model reproduce the positive IMPS signal, and the light JV curve with the same set of model parameters unless we introduced photobleaching. The rational for including photobleaching was that photobleaching will make the device a less efficient absorber of light at higher light intensities. This could result in less charge carriers being generated at higher light intensity than at low light intensity, which would result in the current sinusoid

produced by the device preceding the modulating light signal. To account for this we introduced the photo-bleaching constant ϱ, which is discussed in the main text. The simulated values of Im(J) vs. frequency are plotted for different values of ϱ in fig. S5. It can be seen that large values of ϱ makes the IMPS measurement more sensitive to changes in carrier population at low frequency.
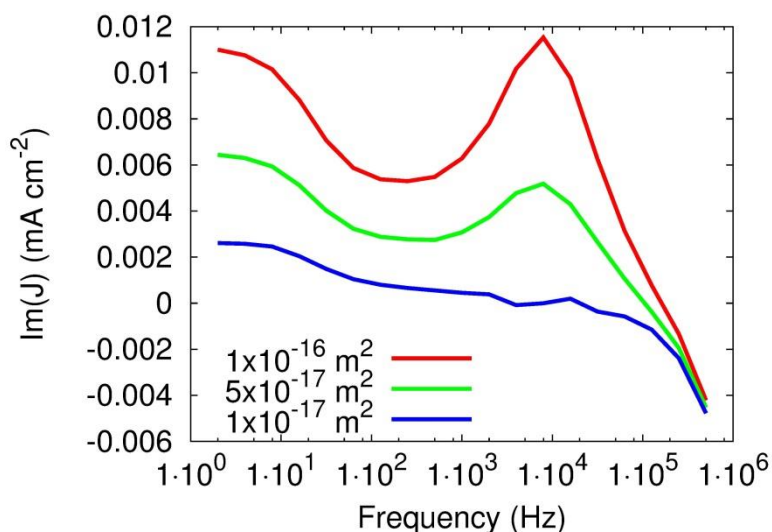

Figure S5 Simulated values of Im(J) vs. frequency for varying values of the photo-bleaching constant ρ

[1] A. Guerrero, N. F. Montcada, J. Ajuria, I. Etxebarria, R. Pacios, G. Garcia-Belmonte and E. Palomares, *J. Mater. Chem. A,* 2013, **1**, 12345.

[2] B. Ecker, R. Steim, H. J. Egelhaaf, J. Parisi and E. von Hauff, *J. Phys. Chem.*, 2012, **116**, 16333.

[3] C. Hoi, Y. Ho, Q. Dong, H. Yin, W. W. K. Leung, Q. Yang, H. K. H. Lee, S. W. Tsang, S. K. So, Adv. Mater. Interfaces, 2015, **2**, 1500166.